Advanced Steel Construction – Vol. 22 No. 2 (2026) 170–180
DOI:10.18057/IJASC.2026.22.2.4

INFLUENCE OF WELDING RESIDUAL STRESS ON AXIAL MECHANICAL PROPERTIES OF HOLLOW SPHERICAL JOINTS

Ren-Zhang Yan [1,*], Hao-Ping Ji [1], Shuai Wang [2], Xiao-Qiang Jin [1] and Lin Song [3]

[1] *School of Civil Engineering, Chongqing Jiaotong University, Chongqing 400074, China*
[2] *Chongqing Aerospace Polytechnic, Chongqing 400021, China*
[3] *China Metallurgical Construction Engineering Group Co., LTD, Chongqing 400037, China*
**(Corresponding author: E-mail: rz_yan@cqjtu.edu.cn)*

ABSTRACT

Significant welding residual stresses (WRS) exist at the sphere-pipe welds of welded hollow spherical joints (WHSJ), adversely affecting their axial mechanical performance. However, due to the complex distribution pattern of residual stress, quantitatively assessing their impact on joint axial stiffness and load-bearing capacity has been challenging. This study employs a combined approach of theoretical derivation and model testing to examine and reveal the influence mechanisms and quantitative influence patterns of sphere-to-pipe welding residual stress on the axial mechanical properties of hollow spherical joints. It was found that welding residual stress reduces joint axial stiffness by 1.97% – 54.7% and load-bearing capacity by 2.27% – 24.4%. Furthermore, the detrimental effect of welding residual stress on axial performance decreases with increasing hollow sphere diameter (D), increases with increasing wall thickness (t), and exhibits a contrasting trend with increasing steel pipe diameter (d): its effect on axial stiffness initially increases then decreases, whereas its effect on load-bearing capacity initially decreases then increases.

ARTICLE HISTORY

Received: 18 February 2025
Revised: 2 July 2025
Accepted: 18 July 2025

KEYWORDS

Welded hollow spherical joints;
Welding residual stress;
Axial stiffness;
Axial compressive capacity;
Experimental study

1. Introduction

Welded hollow spherical joints (WHSJ), developed by Professor Liu X.L.(1991), have been widely used in various spatial grid structures. These joints consist of a core hollow sphere connected to multiple pipes through welded joints. Notably, the core hollow sphere itself is fabricated by welding two hemispherical shells [1]. However, significant WRS exist at the sphere-pipe butt welds, adversely affecting the axial mechanical properties of the joints. This has prompted extensive research by numerous scholars.In terms of overall structural performance, Wang X.(1996) considers the axial stiffness and bending stiffness of the joints when analyzing the grid of welded spherical joints. Through finite element analysis, it is found that after considering the stiffness of the welded spherical joints, the deflection of the grid structure is reduced, and the influence of the axial stiffness on the deflection is greater than that of the bending stiffness[2]; Zhang J.L.(2003) introduces the stiffness model of WHSJ in the design of geodesic and Cavite reticulated shell structures, and analyzes that the joint stiffness has a significant impact on the buckling load and ultimate load of the structure[3,4]. Kang J.'s(2008) research shows that the structural bearing capacity is reduced after considering joint stiffness in geodesic and saddle reticulated shells with initial defects[5,6]. Li F.(2014) establishes a numerical analysis model of semi-rigid joint cylindrical grid mega-structure and analyzes the static performance of the axial semi-rigid, bending semi-rigid and double semi-rigid structures of joints. It is found that the structural bearing capacity decreased by about 15% after considering the superposition effect of bending stiffness and axial stiffness[7]. Su Y.H.(2005) points out that variations in joint axial stiffness significantly influence the load-bearing capacity of latticed shell structures[8]. These studies show that the stiffness of WHSJ has a non-negligible impact on the overall performance of the structure.

In order to accurately evaluate the stiffness of WHSJ, many scholars have conducted extensive studies on their mechanical properties. Yan X.Y.(2021) explores the axial stiffness, bending stiffness, bearing capacity and ultimate tensile and compressive properties of H-beam WHSJ by combining numerical analysis with experimental studies[9,10];Liu H.B.(2018) investigated the axial performance of H-beam WHSJ, conducting a comprehensive analysis of the effects of material strength, geometric dimensions, and stiffening ribs on joint mechanical properties. The study further proposed corresponding calculation methods[11]; Zhao Z.W.(2021), Han Q.H.(2016) and Yan X.Y.(2019) analyze the axial stiffness and bending stiffness of WHSJ under different stress states, and establish relevant calculation formulas[12-14]; In addition, scholars such as Zhao Z.W.(2018), Lu J.(2018), Huang B.S.(2021) and Liu H.B.(2020) also examine the mechanical properties of WHSJ under extreme conditions such as corrosion, fire and high temperature, and achieve rich research results[15-20].

Due to the structural characteristics of WHSJ, their performance is affected by many factors, and many scholars have also conducted studies on these factors. Luo Y.F.(1995) finds that the joint volume has an important influence on the structural stress and buckling morphology[21]; Dong S.L.(2005) conducts an in-depth study on the bearing capacity of WHSJ, proposes a practical calculation method, and points out that the welding quality at the sphere-pipe butt welds is an important factor for the joint stiffness[22,23]; Liao J.(2010) considers the size and quality of various WHSJ and finds that they have different degrees of influence on the joint stiffness and bearing capacity[24]; Wang X.(2000) not only examines the axial and bending stiffness of joints, but also analyzes the influence of the size of joint region on the stiffness and elastic buckling load of grid structure, and concludes that the joint stiffness is related to many factors such as the stress condition, geometric dimensions, and rod size[25]. In summary, the quality of welds at the sphere-pipe butts of the WHSJ is one of the important factors affecting its performance.

Recent studies have further investigated the residual stress distribution at sphere-to-pipe welds and its structural effects. Zhao Z.W. (2016) employed numerical simulations to analyze how residual stresses influence joint performance and the mechanical properties of single-layer latticed shells. The research demonstrated that residual stresses reduce both joint stiffness and structural load-bearing capacity[26]. Yan R.Z. (2023) established a residual stress distribution model for hollow spherical joint welds, complemented by experimental analyses of its impact on bending performance. The results confirmed that residual stresses adversely affect joint bending stiffness and load-bearing capacity, with the degree of influence varying according to joint geometric size[27,28].This study demonstrates that WRS will reduce the bending stiffness and bearing capacity of joints, and the degree of influence varied with the changes in the structural size of joints.

Through literature review, it is found that the current calculation methods for the axial stiffness and bearing capacity of WHSJ are mainly based on experimental analysis, and the results have certain variations. At the same time, there are few studies that consider the influence of WRS. Therefore, based on the previous studies, this paper further explores the influence of WRS on the axial mechanical properties of WHSJ through a combination of theoretical deduction and experimental studies, and clarifies the influence mechanism of WRS on the axial stiffness and ultimate bearing capacity of joints.

2. Specimen design of welded hollow spherical joint

2.1. Joint design

To ensure the representativeness of the research results, the study selected WHSJ commonly used in engineering, with particular focus on the influence of key parameters: hollow sphere diameter (D), wall thickness (t), and steel pipe diameter (d) on joint axial stiffness and ultimate bearing capacity. Axial performance tests were conducted on five groups of specimens (see Table 1 for

detailed parameters). All specimens employed seamless steel pipes with identical dimensions: 470 mm in length and 6 mm in wall thickness on each side.

When welding the steel pipe and the hollow spheres, a single-pass three-layer arc welding is used to simulate the actual engineering, and the hemispherical butt weld of the hollow spheres is avoided. To facilitate loading application in the welded hollow spherical joint model tests and avoid interference with the hemispherical butt welds of the hollow sphere, the specimens were fabricated by connecting the hollow sphere to two steel pipes at a 180° included angle. A 200mm×200mm loading end plate is set at the end of the steel pipe to connect the support. Fig. 1 is a schematic diagram of the specimen structure, in which the grooved plate is mainly used to arrange the displacement sensor. The hollow spheres and steel pipes of all specimens are made of Q235 steel. During the production of the hollow spheres, the WRS generated by welding the two hemispheres is eliminated through heat treatment and static standing.

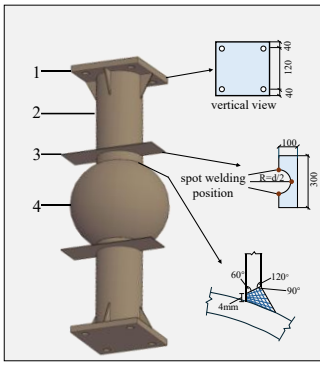

(a) Tectonic diagram
1.fixed end-plate; 2.seamless steel pipe;
3. grooved plates for measuring points;
4.welded hollow sphere.

(b) Photographs of specimens

Fig. 1 Diagram of test pieces

Table 1
Specimen parameters

Number	Specimen number	Ultrasonic impact	Name	*D*/mm	*t*/mm	*d*/mm	Theoretical value of bearing capacity N_R/kN
1	SJ1	No	experiment group	300	8	89	346
	SJ1-D	Yes	control group				
2	SJ2	No	experiment group	350	8	89	329
	SJ2-D	Yes	control group				
3	SJ3	No	experiment group	300	8	114	488
	SJ3-D	Yes	control group				
4	SJ4	No	experiment group	300	10	114	610
	SJ4-D	Yes	control group				
5	SJ5	No	experiment group	300	8	140	656
	SJ5-D	Yes	control group				

Note: Specimens labeled "SJ *i*" (where " *i* " = 1, 2, …, 5) denote the test specimens, with" *i* " indicating the test group index. Correspondingly, "SJ *i*-D" (" *i* "= 1, 2, …, 5) represent the control specimens paired with "SJ *i*". These underwent ultrasonic impact treatment to mitigate WRS immediately after sphere-pipe welding.

2.2. Preparation of control group specimens

To investigate the influence of WRS on the axial performance of the joints, ultrasonic impact method (UIM) was first applied to the sphere-to-pipe welds of the five control group specimens upon completion of fabrication. This treatment aimed to reduce WRS within the welds and the adjacent heat-affected zone. The fundamental principle of UIM involves utilizing high-frequency, high-efficiency, and focused ultrasonic energy to induce sufficient compressive plastic deformation and grain refinement in the metal surface layer. This process alters the WRS field, thereby reducing, homogenizing, or eliminating the residual stresses. In this study, a TY20-80 ultrasonic impact instrument was employed to mitigate WRS in the weld regions. As illustrated in Fig. 2, the UIM treatment involved continuously impacting the weld and heat-affected zone using an impact gun operating at 20,000 Hz, traversing at a uniform speed of 2 cm/min. During the process, the impact gun was maintained perpendicular to the weld, ensuring continuous contact between the impact pin and the weld seam. Detailed test principles and operational procedures are documented in reference [28].Subsequently, to quantify the WRS in all specimens, measurements were taken using an SC21B 3D stress magnetic scanner prior to conducting the axial compression tests. The SC21B scanner operates based on the magnetostrictive effect of ferromagnetic materials, enabling non-destructive measurement of the initial stress within steel components, with a measurement resolution of 1 MPa. The research group had previously conducted relevant UIM and magnetic testing [29].This paper only lists some important results as the basis for the analysis of this paper.

Fig. 2 ultrasonic impact weld process

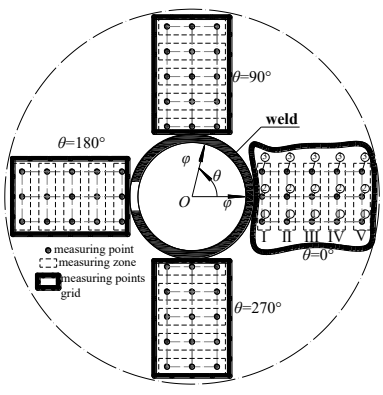

(a)vertical view

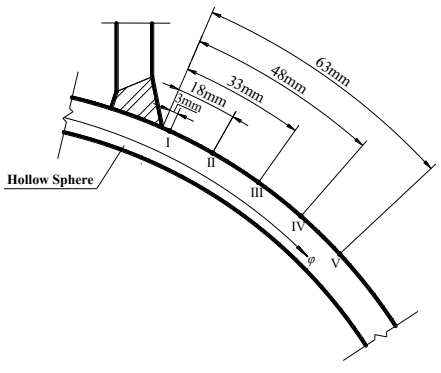

(b)section

Fig. 3 Layout of measuring points of residual stress

Table 2
$\theta = 180$ ° WRS test results

Number	Specimens	Measuring point	Experiment group(SJ*x*)/MPa				Control group(SJ*x*-D)/MPa				β
			$\sigma_{i,\theta}$	$\sigma_{i,\varphi}$	$\sigma_{i,equ}$	$\sum\sigma_{i,equ}$	$\sigma'_{i,\theta}$	$\sigma'_{i,\varphi}$	$\sigma'_{i,equ}$	$\sum\sigma'_{i,equ}$	
1	SJ1 /SJ1-D	I	-26	-96	86	504	-13	-74	68	296	41%
		II	79	-191	241		40	-100	125		
		III	44	-77	106		24	-43	59		
		IV	34	-34	60		19	-22	35		
		V	12	6	11		10	6	9		
2	SJ2 /SJ2-D	I	-29	-82	72	513	-35	-45	41	300	41%
		II	104	-181	249		44	-90	118		
		III	57	-102	139		41	-68	95		
		IV	27	-19	40		21	-17	33		
		V	2	-12	13		2	-12	13		
3	SJ3 /SJ3-D	I	39	-65	91	506	31	-47	68	313	38%
		II	67	-185	225		29	-105	122		
		III	39	-120	143		27	-80	97		
		IV	7	-6	11		7	-7	12		
		V	-7	-39	36		-2	-15	14		
4	SJ4 /SJ4-D	I	-40	-56	50	375	-47	-49	48	248	33%
		II	62	-165	203		44	-83	111		
		III	42	-73	100		29	-58	76		
		IV	3	-12	13		1	-8	9		
		V	10	7	9		5	3	4		
5	SJ5 /SJ5-D	I	-49	-117	102	415	-34	-43	39	296	29%
		II	59	-159	195		42	-92	119		
		III	41	-52	81		38	-45	71		
		IV	28	26	27		36	-26	54		
		V	10	0	10		15	8	13		

Note:
① The number *x* in the table represents the specimen group number, which is 1~5 respectively;
② $\sigma_{i,\theta}$ and $\sigma_{i,\varphi}$ are the circumferential and longitudinal WRS of the test group specimens at the measuring point *i* respectively;
③ $\sigma'_{i,\theta}$ and $\sigma'_{i,\varphi}$ are the circumferential and longitudinal WRS of the control group specimens at the measuring point i respectively;
④$\sigma_{i,equ}$ and $\sigma'_{i,equ}$ are the equivalent WRS of the test group and control group specimens at the measuring point *i* respectively, $\sigma_{i,equ} = \sqrt{(\sigma_{i,\theta})^2 + (\sigma_{i,\phi})^2 - \sigma_{i,\theta} \cdot \sigma_{i,\varphi}}$
⑤ β is the reduction rate of WRS, $\beta = \left(\sum\sigma_{i,equ} - \sum\sigma'_{i,equ}\right) / \sum\sigma_{i,equ}$

When measuring WRS via the magnetic method, a measurement point grid was established on the hollow sphere surface as shown in Fig. 3 to comprehensively characterize the stress distribution pattern. Starting from the weld initiation point, grid units were positioned at 90° intervals along the circumferential direction. Each unit contained five measurement points uniformly spaced longitudinally and three points arranged circumferentially. During measurement, the circumferential stress value at each longitudinal position was determined by averaging the three circumferential measurement points. Due to repeated heating from the welding heat source at the arc-extinguishing point, significant fluctuations occurred in residual stress measurements. Therefore, the measurement grid at $\theta = 180°$ (away from these critical zones) was selected for analysis. Residual stress results for all five specimen groups at this location are presented in Table 2.

It can be seen from Table 2 that ultrasonic impact has a certain effect on eliminating the WRS of the welded hollow spherical joint, which can reduce the WRS of the hollow spherical joint by 29%~41%.

3. Analytical calculation of the influence of WRS on the axial mechanical properties of WHSJ

In order to clarify the influence of WRS on the axial mechanical properties of WHSJ, it is necessary to derive the axial stiffness and bearing capacity of WHSJ analytically before conducting experiments. The research team has established the distribution pattern of WRS of WHSJ in various sizes by using the aforementioned magnetic test and finite element simulation. The relevant results have been reported in detail in[27] This paper will directly use the results to analyze the influence of WRS on the axial mechanical properties of WHSJ.

3.1. Calculation of axial stiffness considering the influence of WRS

The axial stiffness *K* of the joint is the ratio of the axial load *N* to the axial deformation *u* of the joint domain, which can be calculated using Eq. (1). The WHSJ are composite connections formed by welding steel pipes to hollow spherical bodies. The axial deformation within the joint region, denoted as *u*, arises from the combined axial deformation of the steel pipe u_s and the hollow sphere δ_0. Assuming these deformations are independent, the total axial deformation *u* under axial load *N* results from the additive combination of u_s and δ_0 acting in series, as expressed in Eq. (1).

$$K = \frac{N}{u} = \frac{N}{u_s + \delta_0} \tag{1}$$

3.1.1. Joint domain range considering the influence of WRS

The influence of WRS on the joint is mainly concentrated in the sphere-pipe connection weld and the nearby heat-affected zone. Taking SJ1 as an example, Fig. 4 is the WRS distribution pattern diagram of SJ1 established by the research team in the early stage. It can be seen that the maximum WRS appears near the weld, and the WRS in the remaining areas will decrease rapidly as its position moves away from the weld. If 5% of the material yield strength is used as the basis for whether the WRS can be ignored to judge the influence zone of the WRS, the weld affected zone of SJ1 can be obtained as the blue area shown in Fig. 4. At this time, the influence zone height of the steel pipe is h_0 = 106mm, and the influence zone of the hollow spherical shell is $\varphi = 49.83°$.The

WRS distribution pattern of the other specimens is similar to that of SJ1, except that the specific influence range h_0 and φ of each group of specimens will change with the geometric structure size of the joint. Since this paper mainly examines the influence of WRS on the axial bearing performance of the joint, the axial deformation of the joint is mainly calculated in the blue area shown in Fig. 4. Due to space limitations, the following deduction is based on SJ1. The distribution of WRS and the deduction process of the axial mechanical properties of the joints of the other groups of specimens are completely similar to those of SJ1.

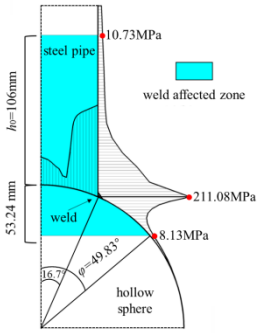

Fig. 4 Pattern of residual stress distribution in SJ1 von Mises welding

3.1.2. Calculation of u_s

To accurately calculate the axial deformation of the welded affected zone of the steel pipe, the distribution law of the axial WRS in the welded affected zone of the steel pipe, i.e., the range of height h_0, should be clarified first. As shown in Fig. 5(a), the axial WRS distribution diagram on the typical section of the steel pipe in SJ1 is shown. Obviously, the axial WRS in the steel pipe is anti-symmetrically distributed along the center of the steel pipe wall thickness (position with r = 41.5mm), and the residual stress is the largest at about 3.5mm from the weld (z = 3.5mm), and the residual stress value has been reduced to less than 10MPa at 100mm from the weld (z = 100mm).

To simplify calculations, the nonlinear axial WRS within the steel pipe is equivalently homogenized as a uniform stress along its thickness direction. As illustrated in Fig. 5(b), the simplification involves dividing the WRS into tensile and compressive zones along the thickness direction based on stress characteristics, with monotonically varying stresses in each zone. The nonlinear stresses in these zones are then homogenized into uniform stresses σ_w using Eq. (2), following the principle of equivalent resultant force. This equivalent treatment preserves the mechanical nature of each zone. Since the resultant force of the equivalent stress matches that of the actual distributed stress, the overall impact remains consistent, ensuring that the influence trend of residual stress on joint mechanical behavior does not deviate significantly. However, applying Eq. (2) for simplification requires identical processing of nonuniform stresses at all height positions along the pipe's longitudinal direction. Fig. 4 reveals that WRS also varies nonlinearly along the pipe height. Accurate computation necessitates discretizing the pipe into numerous segments along its height, resulting in a computationally intensive process. To enhance efficiency, two extreme cases of uniformly distributed residual stress along the height are considered: ① Assume that the axial WRS in the range of height h_0 of the steel pipe is distributed according to the law at z = 3.5mm; ② Assume that the axial WRS in the range of height h_0 of the steel pipe is distributed according to the law at z = 100mm. Although the simplified stress distribution differs from reality, the mechanical nature at each location aligns with actual conditions. The selected stress values represent the maximum and minimum extremes of the actual distribution, bounding the upper and lower limits of the true stress. Consequently, the actual WRS lies between cases ① and ②, and the actual axial deformation u_s within height h_0 must lie between the results computed for these two cases.

$$\sigma_w = \frac{\int_{r=d/2}^{r=d/2+t/2} \sigma \cdot dr}{t/2} \tag{2}$$

In the formula, σ_w is the equivalent uniformly-distributed WRS, σ is the actual WRS, d is the inner diameter of the steel pipe, and t is the wall thickness of the steel pipe. For SJ1, when simplified according to case ①, σ_w = 85.2MPa is calculated, and when simplified according to case ②, σ_w=3.3MPa is calculated.

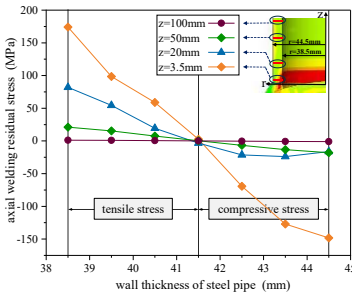

(a) Distribution of axial weld residual stresses in a typical cross-section of steel pipe

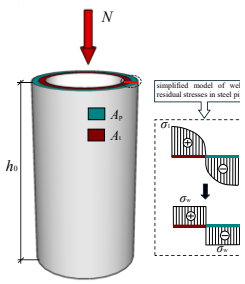

(b) Distribution of weld residual stresses before and after simplification of pipe section

Fig. 5 Residual stress distribution in welded SJ1 steel pipe

After simplification in the above manner, the cross section A within the height range of the steel pipe h_0 will be divided into two parts: The compression circumferential region A_p near the outside and the tension circumferential region A_t near the inside, as shown in Fig. 5(b). Obviously, A=A_p+A_t. When the WRS is not considered, the axial deformation within the height range of the steel pipe h_0 under the action of the axial force N can be calculated according to Eq. (3):

$$u_0 = \frac{Nh_0}{EA} \tag{3}$$

When considering the influence of WRS, if the proportional limit load of the steel pipe is assumed to be N_e, the axial force of the steel pipe under the action of N will go through two stages:

i 0~N_e stage: The entire cross section of the steel pipe is under pressure, that is, the compressive stress in the A_p region is less than the yield strength of the steel at this stage, and can share N with the A_t region. When N reaches N_e, the compressive stress in the A_p region just reaches the yield strength f_y, that is, $N_e/A+\sigma_w=f_y$. At this time, the axial deformation u_1 generated within the height range of the steel pipe h_0 can be calculated according to Eq. (4):

$$u_1 = \frac{N_e h_0}{EA} = \frac{(f_y - \sigma_w)\cdot h_0}{E} \tag{4}$$

ii N_e~N stage: In this stage, the stress value in the A_p region is the steel yield strength f_y, which will no longer increase, and plastic deformation will continue to occur. N is only borne by the A_t region. When the load reaches N, the axial displacement u_2 within the height range of the steel pipe h_0 is calculated according to Eq. (5):

$$u_2 = \frac{(N - N_e)h_0}{EA_t} \tag{5}$$

The axial displacement of the steel pipe during the entire loading process is:

$$u_s = u_1 + u_2 \tag{6}$$

For SJ1, A=1564mm^2, then A_p=A_t=782mm^2, and h_0=106mm, f_y=235N/mm^2, E=2.06×105N/mm^2, when simplified according to the above cases ① and ②, σ_w is 85.2MPa and 3.3MPa respectively. According to Eq. (3), u_0=3.29×10^{-4}×N is obtained for the steel pipe when the influence of WRS is not considered for SJ1.

According to Eqs. (4)-(6), the simplified N_e and u_s of SJ1 according to case ① are:

$$N_e = (f_y - \sigma_w)A = 234.3 \text{ (kN)} \tag{7}$$

$$u_s = 6.58\times10^{-4}\times(N-N_e)+0.08 \text{ (mm)} \tag{8}$$

According to case ②, the simplified N_e and u_s are:

$$N_e = (f_y - \sigma_w)A = 362.4 \text{ (kN)} \tag{9}$$

$u_s = 6.58\times10^{-4}\times(N-N_e)+0.12$ (mm) (10)

3.1.3. Calculation of δ_0

Similarly, to evaluate the influence of WRS on the axial deformation of the hollow sphere, the distribution pattern of residual stress within the spherical shell must first be defined. Following the same procedure applied to simplify u_s, the WRS in the hollow spherical joint is partitioned into distinct zones based on tensile and compressive characteristics, with stresses in each zone homogenized into uniform values.

Since the longitudinal and circumferential stresses in the hollow spherical shell will cause the vertical deformation, the distribution patterns of WRS in the hollow spherical shell along two directions are first extracted. As shown in Figs. 6(a)-(b), they are the distribution characteristics of longitudinal and circumferential WRS in the SJ1 hollow spherical shell established by the research team in the early stage. It can be seen that the WRS in the SJ1 hollow spherical shell has the following distribution law: the longitudinal WRS is roughly anti-symmetrically distributed along the wall thickness direction of the sphere with the center line of the wall thickness, that is, within the range of φ=0°~36°, the longitudinal WRS is transformed from tension to compression from the inner surface to the outer surface of the hollow sphere, and the maximum value is obtained at φ=27°, while in the range of φ=36°~90°, the opposite is true; the distribution of circumferential WRS along the wall thickness direction is mainly compressive stress inside and outside the circumferential seam, and the maximum value is obtained at φ=31°. Section 3.1.1 has made it clear that the influence zone of the SJ1 hollow spherical shell is within the range of φ=49.83°. As with the deformation analysis of steel pipes, the maximum residual stress and the minimum residual stress within the influence zone are taken for analysis. Specifically, when considering the most adverse effect of WRS, it is assumed that the WRS within the influence zone of the hollow sphere is uniformly distributed, and the longitudinal and circumferential WRS are distributed according to the conditions at φ=27° and φ=31° respectively; when considering the minimum effect of WRS, the longitudinal and circumferential WRS within the influence zone are distributed according to the conditions at φ=36° and φ=49° respectively, as shown in Fig. 6(c). To simplify the analysis, the longitudinal and circumferential residual stresses are simplified to the uniform distribution mode shown in Fig. 6(d) according to the principle that the tensile and compressive forces are equivalent.

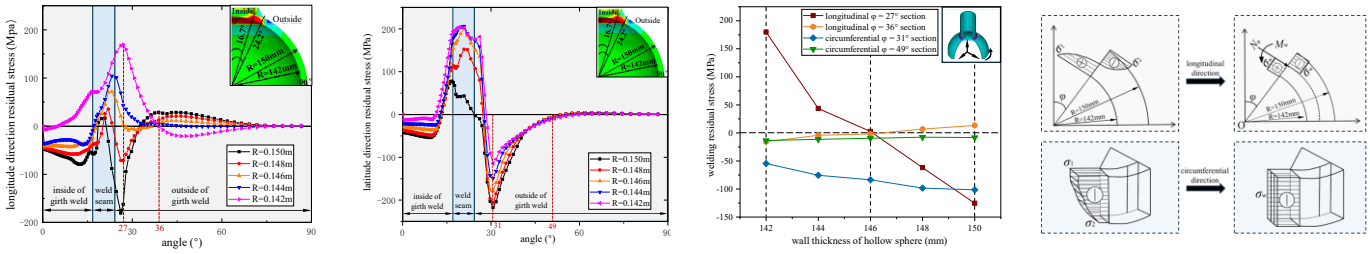

(a) WRS along the wall thickness of the SJ1 shell in the longitudinal direction

(b) Residual weld stress in the circumferential direction along the wall thickness of SJ1 spherical shells

(c) WRS distribution in a typical cross-section of a SJ1 spherical shell

(d) simplified weld residual stress distribution in the meridional and circumferential sections of the spherical shells

Fig. 6 Residual stress distribution of welded SJ1 spherical shells

The hollow sphere is mainly subjected to the axial force N transmitted by the steel pipe. Since the rigidity of the steel pipe and the surrounding spherical shell is relatively large, in order to simplify the analysis, the spherical shell within the steel pipe is regarded as a rigid body[23]. The internal force of the axial force N in the spherical shell can be decomposed into the longitudinal and circumferential membrane forces N_φ and N_θ, the bending moments M_φ and M_θ rotating around N_φ and N_θ, and the transverse shear force Q_φ pointing to the center of the sphere, and the longitudinal and circumferential shear forces S_φ and S_θ. Since the hollow sphere is highly symmetrical, S_φ and S_θ are both equal to 0. If the change of internal force along the thickness direction of the spherical shell is ignored and the mid-surface of the spherical shell is taken as the surface of internal force action, the distribution of internal force of the spherical shell is shown in Fig. 7, and the relationship between N and each internal force can be expressed by Eqs. (11)-(15)[13].

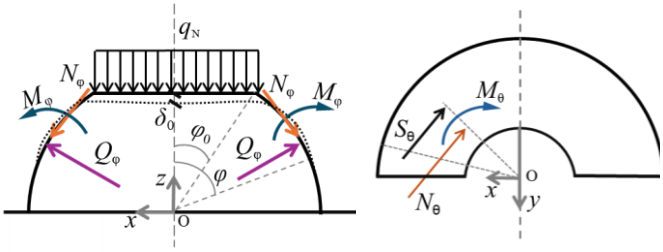

(a) Internal force distribution profile of a spherical shell

(b) Top view of internal force distribution in a spherical shell

Fig. 7 Distribution of internal forces in the spherical shell

$$N_\varphi = \frac{(1+\mu)N\cot\varphi}{\beta_s\sin\varphi_0}\cdot e^{\beta_s(\varphi_0-\varphi)}\cdot(\cos\beta_s\varphi_0\cos\beta_s\varphi+\sin\beta_s\varphi_0\sin\beta_s\varphi)-\frac{N\sin\varphi_0}{\sin^2\varphi} \tag{11}$$

$$N_\theta = \frac{(1+\mu)N}{\sin\varphi_0}\cdot e^{\beta_s(\varphi_0-\varphi)}\cdot[(\cos\beta_s\varphi_0-\sin\beta_s\varphi_0)\cos\beta_s\varphi+(\cos\beta_s\varphi_0+\sin\beta_s\varphi_0)\sin\beta_s\varphi]+\frac{N\sin\varphi_0}{\sin^2\varphi} \tag{12}$$

$$Q_\varphi = -\frac{(1+\mu)N}{\beta_s\sin\varphi_0}\cdot e^{\beta_s(\varphi_0-\varphi)}\cdot(\cos\beta_s\varphi_0\cos\beta_s\varphi+\sin\beta_s\varphi_0\sin\beta_s\varphi) \tag{13}$$

$$M_\varphi = \frac{(1+\mu)DN}{4\beta_s^2\sin\varphi_0}\cdot e^{\beta_s(\varphi_0-\varphi)}\cdot[(\cos\beta_s\varphi_0+\sin\beta_s\varphi_0)\cos\beta_s\varphi+(\sin\beta_s\varphi_0-\cos\beta_s\varphi_0)\sin\beta_s\varphi] \tag{14}$$

$$M_\theta = \frac{\mu(1+\mu)DN}{4\beta_s^2\sin\varphi_0}\cdot e^{\beta_s(\varphi_0-\varphi)}\cdot[(\cos\beta_s\varphi_0+\sin\beta_s\varphi_0)\cos\beta_s\varphi+(\sin\beta_s\varphi_0-\cos\beta_s\varphi_0)\sin\beta_s\varphi] \tag{15}$$

In the formula, $\beta_S=\sqrt[4]{\frac{3\left(1-\mu^2\right)D^2}{4t^2}}$; φ_0 is the opening angle at the top of the spherical shell, that is, the surrounding range of the steel pipe; μ is the Poisson's ratio, D is the outer diameter of the spherical shell; t is the wall thickness of the hollow sphere.

According to the theory of elastic thin shell , the work done by the internal forces N_φ, N_θ, M_φ, M_θ, and Q_φ of the hollow spherical shell in their respective directions can be expressed as:

$$W_{N_\varphi}=\int_0^{2\pi}\int_0^{\frac{\pi}{2}}\frac{1}{Et}\left(N_\varphi^2-\mu N_\varphi N_\theta\right)A_1A_2\cdot d\theta d\varphi \tag{16}$$

$$W_{N_\theta}=\int_0^{2\pi}\int_0^{\frac{\pi}{2}}\frac{1}{Et}\left(N_\theta^2-\mu N_\varphi N_\theta\right)A_1A_2\cdot d\theta d\varphi \tag{17}$$

$$W_{Q_\varphi}=\int_0^{2\pi}\int_0^{\frac{\pi}{2}}\frac{2(1+\mu)}{Et}Q_\varphi^2A_1A_2\cdot d\theta d\varphi \tag{18}$$

$$W_{M_\varphi}=\int_0^{2\pi}\int_0^{\frac{\pi}{2}}\frac{12}{Et^3}\left(M_\varphi^2-\mu M_\varphi M_\theta\right)A_1A_2\cdot d\theta d\varphi \tag{19}$$

$$W_{M_\theta}=\int_0^{2\pi}\int_0^{\frac{\pi}{2}}\frac{12}{Et^3}\left(M_\theta^2-\mu M_\varphi M_\theta\right)A_1A_2\cdot d\theta d\varphi \tag{20}$$

In the above formula, A_1 and A_2 are Lame coefficients. In the spherical shell, $A_1=D/2$, $A_2=(D/2)\cdot\sin\varphi$, and E is the elastic modulus.

According to Fig. 7(a), when the upper boundary of the hollow spherical shell produces a vertical displacement of δ_0, according to the principle of virtual work:

$$N\delta_0=W_{N_\varphi}+W_{N_\theta}+W_{Q_\varphi}+W_{M_\varphi}+W_{M_\theta}$$

Combining the above formulas, the vertical displacement δ_0 of the hollow spherical shell under the axial load N can be solved as:

$$\delta_0=\left\{\int_0^{2\pi}\int_0^{\frac{\pi}{2}}\left[\frac{1}{Et}\left(N_\phi^2-\mu N_\phi N_\theta\right)+\frac{1}{Et}\left(N_\theta^2-\mu N_\phi N_\theta\right)+\frac{12}{Et^3}\left(M_\phi^2-\mu M_\phi M_\theta\right)+\frac{12}{Et^3}\left(M_\theta^2-\mu M_\phi M_\theta\right)+\frac{2(1+\mu)}{Et}Q_\phi^2\right]A_1A_2d\theta d\phi\right\}\times\frac{1}{N} \tag{21}$$

Assume that the internal forces in the spherical shell caused by WRS are $N_{w\varphi}$, $N_{w\theta}$, $M_{w\varphi}$, $M_{w\theta}$, $Q_{w\varphi}$, $S_{w\varphi}$, and $S_{w\theta}$ respectively. Now SJ1 is taken as an example to illustrate the calculation method considering the influence of WRS.

After the WRS is simplified in the above way, the calculation of N_φ work considering the influence of $N_{w\varphi}$ can refer to the calculation idea of steel pipe in Section 3.1.2, that is, the cross section $A_{s\varphi}$ within the t thickness range of the spherical shell is divided into two areas: The compression circumferential area $A_{p\varphi}$ close to the outside and the tension circumferential area $A_{t\varphi}$ close to the inside, as shown in Fig. 6(d), $A_{s\varphi}=A_{p\varphi}+A_{t\varphi}$. When considering the influence of WRS, assuming that the proportional limit load of the spherical shell longitudinal membrane force is $N_{e\varphi}$, the spherical shell force under the action of the longitudinal force N_φ will go through two stages:

i 0~$N_{e\varphi}$ stage: The entire cross section of the spherical shell is compressed in the longitudinal direction, that is, the compressive stress in the $A_{p\varphi}$ region at this stage is less than the yield strength of the steel, and can share N_φ with the $A_{t\varphi}$ region. When N_φ reaches $N_{e\varphi}$, the compressive stress in the $A_{p\varphi}$ region just reaches the yield strength f_y, that is, $N_{e\varphi}/A_{s\varphi}+\sigma_{w\varphi}=f_y$. At this stage, the work done by N_φ is calculated according to Eq. (22):

$$W_1=\int_0^{2\pi}\int_0^{\frac{\pi}{2}}\frac{1}{Et}\left(N_{e\varphi}^2-\mu N_{e\varphi}N_\theta'\right)A_1A_2\cdot d\theta d\varphi \tag{22}$$

ii $N_{e\varphi}$~N_φ stage: In this stage, the stress value of the $A_{p\varphi}$ region is the steel yield strength f_y, and the resultant force $N_p=f_yA_{p\varphi}$ no longer increases. Plastic deformation will continue to occur, and N_φ is only borne by the $A_{t\varphi}$ region. In this stage, the work done by N_φ consists of two parts: the elastic region and the plastic region, which can be calculated according to Eq. (23):

$$W_2=\int_0^{2\pi}\int_0^{\frac{\pi}{2}}\left\{\frac{2}{Et}\left[\left(N_\varphi-N_{e\varphi}\right)^2-\mu\left(N_\varphi-N_{e\varphi}\right)N_\theta'\right]+\frac{2}{Et}\left(N_p^2-\mu N_pN_\theta'\right)\right\}A_1A_2\cdot d\theta d\varphi \tag{23}$$

Among them , as shown in Fig. 6(d), the simplified circumferential WRS is uniformly distributed in the same direction, so $N_{w\theta}=\sigma_{w\theta}A_{s\theta}$.Then the work N_φ considering the WRS can be calculated according to Eq. (24):

$$W_{N_\varphi}=W_1+W_2 \tag{24}$$

As shown in Fig. 6(d), the simplified resultant force of the longitudinal WRS is almost 0, and the effect on the work done by the circumferential WRS can be ignored. Therefore, the work done by N_θ considering the WRS can be calculated according to Eq. (25):

$$W_{N_\theta}=\int_0^{2\pi}\int_0^{\frac{\pi}{2}}\frac{1}{Et}\left[\left(N_\theta+N_w\right)^2-\mu N_\varphi\left(N_\theta+N_w\right)\right]A_1A_2\cdot d\theta d\varphi \tag{25}$$

In the theoretical analysis, the influence of the wall thickness of shell on the internal force is ignored, and it is assumed that all internal forces act on the mid-surface of the shell. As shown in Fig. 6(d), the longitudinal WRS $\sigma_{w\varphi}$ is distributed anti-symmetrically on the mid-surface of the shell. According to the moment balance principle, there must be a bending moment $M_{w\varphi}$ caused by $\sigma_{w\varphi}$ at the φ section, and its magnitude can be calculated according to Eq. (26):

$$W_{M_\varphi}=\frac{1}{4}t\sigma_{w\varphi}A_s\varphi \tag{26}$$

As shown in Fig. 6(d), the circumferential WRS does not cause bending moment on the mid-surface of the spherical shell and there is no distribution of tangential WRS , so $M_{w\theta}=Q_{w\varphi}=S_{w\varphi}=S_{w\theta}=0$. When the WRS of spherical shell is considered, the vertical displacement δ'_0 of the spherical shell can be calculated according to Eq. (27):

$$\delta_0'=\frac{W_{N_\varphi}+W_{N_\theta}+W_{M_\varphi}}{N} \tag{27}$$

For SJ1, D=300mm, t=8mm, φ_0=16.7°, β_s=5.57, f_y=235N/mm^2, $A_{s\theta}$=1833.76mm^2, $A_{s\varphi}$=3315.84mm^2, and $A_{p\varphi}=A_{t\varphi}$ =1657.92mm^2, considering that the residual stress value of the φ=27° section is relatively large, in order to facilitate the solution, the internal force of this section is taken for quantitative analysis. Then according to Eqs. (11)-(15), the internal force of the spherical shell at the φ=27° section of SJ1 without considering the influence of WRS is calculated: $\varphi=-1.38\times N$, $N_\theta=1.38\times N$, $M_\varphi=-3.84\times N\times10^{-25}$, $M_\theta=-1.15\times N\times10^{-25}$, and $Q_\varphi=-0.52\times N\times10^{-25}$. Since the values of M_φ、M_θ, and Q_φ are all small, their influence on the axial stiffness of the spherical shell can be ignored, and $M_\varphi=M_\theta=Q_\varphi=0$ can be directly assumed. Then, according to Eq. (27), when the WRS is not considered, the spherical shell $\delta_0=2.36\times10^{-3}\times N$ is obtained.

According to the simplified method mentioned above, when considering the influence of the maximum WRS: $\sigma_{w\varphi}=63.9$MPa, $\sigma_{w\theta}=-83.62$MPa, $N_{e\varphi}=(f_y-\sigma_{w\varphi})A_{s\varphi}=567.34$(kN), and $N_\theta'=N_\theta+\sigma_{w\theta}A_{s\theta}=1.38\times N-153.34$, then according to Eq. (27), $\delta'_0=3.2\times10^{-3}\times N+0.21$ is calculated; When considering the influence of the minimum WRS: $\sigma_{w\varphi}=6.43$MPa, $\sigma_{w\theta}=-9.87$MPa, $N_{e\varphi}=(f_y-\sigma_{w\varphi})A_{s\varphi}=758$(kN), and $N_\theta'=N_\theta+\sigma_{w\theta}A_{s\theta}=1.38\times N-18.1$, then according to Eq. (27), $\delta'_0=2.41\times10^{-3}\times N+0.12$ is calculated.

3.1.4. Calculation of K

When considering the distribution of maximum WRS of SJ1, the spherical

shell $N_{c\varphi}$ is 567.34kN. During the loading process, the longitudinal force of the spherical shell is always in the elastic stage, while the steel pipe N_e is only 234.3kN. Therefore, it is advisable to take the theoretical bearing capacity of joint N=346kN to make a quantitative analysis of the axial stiffness of joint. When the WRS is not considered, the vertical displacement of the steel pipe u_0=3.29×N×10^{-4} = 0.11(mm), the vertical displacement of the spherical shell δ_0=2.36×N×10^{-3} = 0.82(mm), and the axial stiffness of the joint is:

$$K_0 = \frac{N}{u_0 + \delta_0} = 3.72\times10^5 (\mathrm{N/mm}) \tag{28}$$

When considering the influence of the maximum WRS, the vertical displacement of the steel pipe is u_s = 6.58×10^{-4}×(N-N_e)+0.08 = 0.15(mm), and the vertical displacement of the spherical shell is δ'_0=3.2×N×10^{-3}+0.21 = 1.32(mm), then the axial stiffness of the hollow joint is:

$$K_1 = \frac{N}{u_0 + \delta_0} = 2.35\times10^5 (\mathrm{N/mm}) \tag{29}$$

When considering the influence of the minimum WRS, the vertical displacement of the steel pipe is u_s = u_0 = 3.29×N×10^{-4}=0.11 (mm), and the vertical displacement of the spherical shell is δ'_0 = 2.41×10^{-3}×N+0.08 = 0.91(mm), then the axial stiffness of the joint is:

$$K_2 = \frac{N}{u_0 + \delta_0} = 3.39\times10^5 (\mathrm{N/mm}) \tag{30}$$

The maximum weakening degree β_k of the axial stiffness of the SJ1 joint caused by WRS is 36.8%, and the minimum weakening degree β_k is 8.9%. That is, the theoretical weakening degree of the axial stiffness of the SJ1 joint caused by WRS is between 8.9% and 36.8%.It should be noted that the aforementioned computational procedure simplifies the distribution pattern of WRS, assuming uniform distributions of key stress values at the extreme minimum and maximum levels within the joint region. While the resulting range of joint stiffness reduction bounds the actual scenario, this range is conservatively broad. The computational process for all other specimen groups (e.g., SJ2–SJ5) follows an identical approach to SJ1 and is thus omitted here.

3.2. Influence of WRS on ultimate bearing capacity of joints

Assuming that the welded hollow spherical joint mainly suffers from punching shear failure under axial load, and the vertical shear stress τ plays a controlling role on the punched surface, the joint will suffer from punching shear failure when the shear stress on the punching surface reaches the yield strength[23], as shown in Fig. 8. According to the von-Mises equivalent stress theory, when the equivalent stress of the shear stress on the punched surface exceeds the yield strength of the material, the joint is considered to be damaged. In order to analyze the influence mechanism of WRS on the ultimate compressive bearing capacity of the hollow spherical joint, a micro-segment is taken on the circumferential punched surface of the hollow spherical joint for analysis, as shown in Fig. 9.

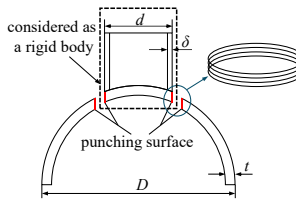

Fig. 8 Schematic diagram of punching damage of welded hollow sphere joint

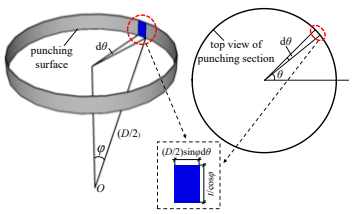

Fig. 9 Schematic diagram of punched surface differential segments

Assume N_u is the ultimate bearing capacity. From the geometric relationship, the length of the micro-segment is t/cosφ and the width is (D/2)sinφdθ. The stress resultant on the micro-segment can be calculated according to Eq. (31). Then, it is integrated along the circumferential direction of the hollow spherical joint. The theoretical ultimate bearing capacity of the joint based on the shear stress destruction model of the punched surface can be calculated according to Eq. (32).

$$\mathrm{d}N_u = \tau\left(\frac{t}{\cos\varphi}\right)\left(\frac{D}{2}\right)\sin\varphi\mathrm{d}\theta \tag{31}$$

$$N_u = \int_0^{2\pi}\tau\left(\frac{t}{\cos\varphi}\right)\left(\frac{D}{2}\right)\sin\varphi\mathrm{d}\theta = \tau\pi D\tan\varphi = \frac{f_y}{\sqrt{3}}\pi D\tan\varphi \tag{32}$$

Assume that N_w represents the resultant force of WRS on the punched surface, and similarly it can be calculated according to Eq. (33):

$$N_w = \int_0^{2\pi}\tau_w\left(\frac{t}{\cos\varphi}\right)\left(\frac{D}{2}\right)\sin\varphi\mathrm{d}\theta = \tau_w\pi D\tan\varphi \tag{33}$$

In the formula: τ_w is the equivalent tangential residual stress on the punched surface.

When WRS exists on the punched surface, the maximum bearing capacity of WHSJ can be calculated by Eq. (34):

$$N'_u = N_u - N_w \tag{34}$$

The degree of weakening of the ultimate bearing capacity of Welded hollow spherical joints by WRS β_N can be calculated by Eq. (35):

$$\beta_N = \frac{N_u - N'_u}{N_u}\times100\% \tag{35}$$

Based on the previous studies of the research group, the data of tangential WRS on the SJ1 punched surface are extracted and the distribution curve is drawn as shown in Fig. 10. It can be seen that the tangential residual stress on the punched surface changes with the thickness in a gradient manner. The closer to the weld, the larger the value is, and the maximum value appears at the starting point of welding. Except for the starting point of welding, the tangential WRS is basically equal. The WRS of each layer is regarded as the same value, and the equivalent tangential WRS of the punched surface of this layer is taken as the principle of equal resultant force of the layer. To simplify the calculation, two extreme cases are analyzed: ① Assume that the tangential WRS on the punched surface is distributed according to the law of the welding layer; ② Assume that the tangential WRS on the punched surface is distributed according to the law at a distance t from the welding layer. Of course, the actual distribution law of WRS on the punched surface is also between ① and ②, and the impact on the ultimate bearing capacity of the joint is also between ① and ②. It is worth noting that the calculation formula for the bearing capacity of joint given by Eq. (34) is completely based on theoretical derivation and lacks experimental correction. The calculation result may not be completely consistent with the actual situation, but it can reflect the impact trend to a certain extent and provide guidance for the experimental research in this paper.

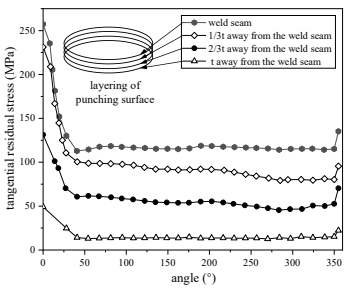

Fig. 10 Residual weld stress distribution in the tangential direction on the punched surface of SJ1

For SJ1, when simplified according to the above cases ① and ②, τ_w is 118.4MPa and 14.3MPa respectively. According to Eq. (33), the resultant force N_w of WRS on the SJ1 punched surface is 267.7kN and 32.3kN respectively. According to Eq. (32), the ultimate bearing capacity of joint N_u is 306.7kN when the WRS is not considered. According to Eq. (34), the maximum bearing capacity N_u' of SJ1 is 39kN and 274.4kN respectively. According to Eq. (35), β_N is 87.2% and 10.5% respectively. According to the calculation results, the

theoretical weakening degree of WRS on the ultimate bearing capacity of SJ1 joint will be between 10.5% and 87.2%.

4. An experimental study on axial bearing performance of WHSJ

Given the nonlinear distribution of WRS within the joint and the coexistence of tensile and compressive stresses, the preceding theoretical calculations employed necessary approximations. While these simplifications capture the influence trend of WRS on the axial load-bearing behavior of WHSJ, they cannot quantify its magnitude. To rigorously assess the quantitative impact of WRS on joint axial performance, an experimental investigation on the axial behavior of WHSJ was conducted.

4.1. Test design of axial loading

4.1.1. Loading plan

In order to simulate the axial force of the joint, two sets of hinged supports are designed to be connected to the loading end plates of the upper and lower ends of the specimen by bolts, then the upper hinged support is connected to the reaction frame crossbeam by screws, and a pressure sensor is placed between the hinged support and the crossbeam; the lower hinged support is directly placed on a 200-ton pneumatically controlled hydraulic jack, as shown in Fig. 11, which is a diagram of the test loading device.

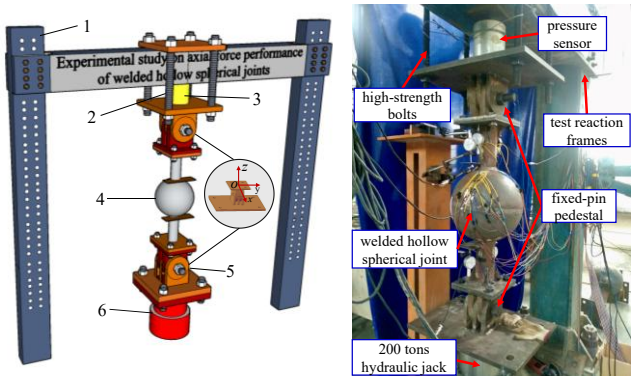

(a) Schematic diagrams test reaction frames;2.high-strength bolts; 3.pressure sensor; 4.welded hollow spherical joint; 5.fixed-pin pedestal;6. 200 tons hydraulic jack

(b) Photographs of loading device diagram

Fig. 11 Loading device diagram

The test loading adopts monotonic static loading. Reference [31]calculates the theoretical axial compressive bearing capacity N_R of each group of specimens according to Eq. (36), which is listed in Table 1 of Section 2.1. Since N_R has taken into account a certain degree of safety, the actual loading load P=1.6N_R is taken, and the loading is divided into 14 levels. Before loading to 0.6P, it increases step by step by 0.1P; after 0.6P, it increases step by step by 0.05P to capture the destruction mode of the joint. Before formal loading, it is preloaded to 0.4P and then unloaded to eliminate the gap between the specimen and the loading system.

$$N_R = \eta_0\left(0.29 + 0.54\frac{d}{D}\right)\pi t d f \tag{36}$$

In the formula: η_0 is the adjustment coefficient of bearing capacity of large-diameter hollow spherical joint, when D≤500mm, η_0=1.0; f is the design value of steel strength, f=215N/mm^2.

4.1.2. layout of measuring points

In order to obtain the axial bearing performance of the joint, the axial deformation of the joint during the loading process should be measured. Therefore, four groups of displacement meters are arranged on the joint according to Fig. 12. At this time, the axial displacement w of the joint can be calculated according to Eq. (37).

$$w = (w_3 + w_4)/2 - (w_1 + w_2)/2 \tag{37}$$

In the formula: w_1~w_4 are the axial deformation values measured by 4 groups of displacement meters.

Since there are certain errors in the specimen production and loading device, eccentricity is inevitable during the loading process. In order to examine the eccentricity of each group of specimens, 4 groups of strain gauges are symmetrically arranged on the upper and lower steel pipes; at the same time, in order to track the stress changes of the joint during the loading process, strain rosettes are arranged on the WHSJ, as shown in Fig. 12.

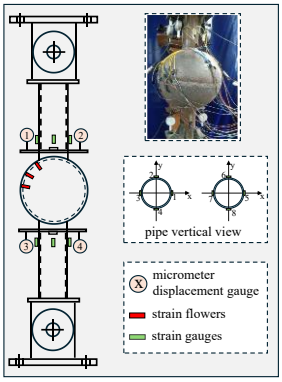

Fig. 12 Layout of measurement points

4.2. test results

4.2.1. Load-displacement curve

The axial deformation of each group of specimens during the loading process is extracted and calculated, and its variation curve along the loading process is plotted, as shown in Fig. 13.

As can be seen from Fig. 13, the axial deformation of each group of specimens changes similarly during the loading process, and their load-displacement curves can be divided into the elastic stage, the elastoplastic stage, and the descending stage. Taking SJ1 as an example, in the initial stage of loading, that is, when the axial displacement increases from 0 to about 1 mm, the axial deformation of the joint increases linearly with the load, and the joint is in the elastic stage as a whole; When the load increases to 208 kN, that is, 0.6P, the joint deformation changes nonlinearly with the load, the displacement increase rate is greater than the load increase rate, and the joint enters the elastoplastic stage; When the load increases to 255 kN, that is, about 0.7P, the joint will enter the plastic stage, and the plastic zone will continue to expand. Even if the load is reduced, the deformation will continue to increase, and then the joint will be damaged.

In addition, as shown in Fig. 13, the load-displacement curves of the control specimens exhibit steeper slopes in the elastic stage than those of the test specimens, indicating higher axial stiffness. Concurrently, the control group demonstrates greater peak loads, confirming superior ultimate load-bearing capacity. These results verify that WRS undermines both the axial stiffness and ultimate bearing capacity of the joints.

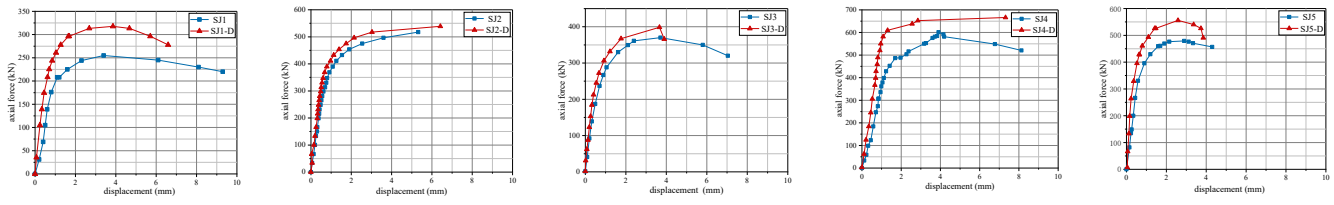

SJ1 & SJ1-D SJ2 & SJ2-D SJ3 & SJ3-D SJ4 & SJ4-D SJ5 & SJ5-D

Fig. 13 Load-displacement curve

4.2.2. Axial stiffness and ultimate bearing capacity of joint

To quantify the influence of WRS on the axial mechanical properties of WHSJ, the elastic axial stiffness and ultimate compressive capacity were extracted from test and control specimens using a graphical method. Taking SJ1 and SJ1-D as examples (Fig. 14): First, fit the load-displacement curve and draw a horizontal line through the peak load point to determine the ultimate capacity N_u. Then, draw a tangent to the elastic segment from the origin, intersecting the peak horizontal line at points A and B. The slopes OA and OB represent the elastic axial stiffness K and K_{Urr}, respectively. The parameters for all specimen groups, calculated via this method, are listed in Table 3. For comparative analysis, Table 3 also includes theoretical values of the axial stiffness and ultimate capacity reduction rates for the five specimen groups.

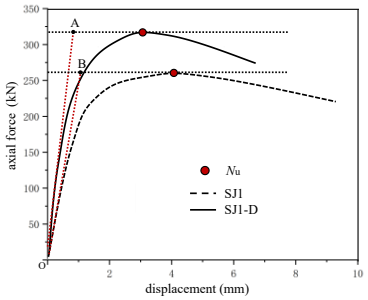

Fig. 14 Calculation of axial stiffness and ultimate compressive load capacity of hollow sphere joint by graphical method

Table 3
Experiment results of axial mechanical properties

number	test specimen	test values K(10^3N/mm)	test values N_u(kN)	control specimen	test values K_{Urr} (10^3N/mm)	test values N_{Urr} (kN)	β_K		β_N	
							test results	theoretical results	test results	theoretical results
1	SJ1	206.11	255.24	SJ1-D	249.8	317.63	21.24%	8.9%~36.8%	24.44%	10.5%~87.2%
2	SJ2	400.18	517.57	SJ2-D	457.8	538.84	14.40%	10.5%~41.7%	4.11%	3.46%~85.2%
3	SJ3	271.24	389.62	SJ3-D	333.03	398.46	22.78%	11.5%~39.6%	2.27%	4.1%~86.3%
4	SJ4	377.9	601.2	SJ4-D	584.6	666.46	54.7%	11.5%~57.3%	10.85%	10.17%~88.8%
5	SJ5	447.88	479.28	SJ5-D	456.69	555.86	1.97%	6.7%~61.1%	15.98%	11.2%~88.2%

Note: ① K in the table is the elastic axial stiffness of the joints in the test group, and K_{Urr} is the elastic axial stiffness of the joints in the control group; ② N_u in the table is the ultimate bearing capacity of the joints in the test group, and N_{Urr} is the ultimate bearing capacity of the joints in the control group; ③ β_K is the weakening rate of axial stiffness, $\beta_K = \frac{(K_{Urr} - K)}{K} \times 100\%$; ④ β_N is the weakening rate of ultimate bearing capacity, $\beta_N = \frac{(N_{Urr} - N_u)}{N_u} \times 100\%$.

1) Effect of WRS on axial mechanical properties of joints

As indicated in Tables 2 and 3, a 30%–40% reduction in WRS in the test specimens enhances the axial stiffness of WHSJ by approximately 1.97%–54.7% and increases their ultimate bearing capacity by approximately 2.27%–24.44%. Compared to theoretical derivation, the experimental results exhibit generally lower values. This discrepancy stems from simplifications in the theoretical model: WRS throughout the joint were partitioned into distinct tensile and compressive zones, with nonlinear stresses in each zone homogenized into uniform values. Additionally, ultrasonic impact treatment failed to achieve complete elimination of WRS in control specimens, resulting in partially retained stresses that further contributed to the reduced experimental values.

Specifically, the axial stiffness of the SJ1 joint increased by 21.24%, and the ultimate bearing capacity increased by 24.44%. The degree of influence is consistent with the influence range of theoretical derivation , indicating that the WRS does affect the axial mechanical properties of the hollow spherical joint, but the specific degree of influence is relatively discrete. In particular, when the WRS of the two groups of specimens 1 and 2 in Table 3 is reduced by 41%, the increase degree of the axial stiffness and ultimate bearing capacity of the joint is quite different. The reason is mainly because the sphere diameters D of the two groups of specimens 1 and 2 are different. Obviously, the structural dimensions of the joint will affect the distribution of WRS, and then the degree of influence on the axial mechanical properties of the joint will also be affected. The other groups of specimens also showed similar situations, which shows that the degree of influence of WRS on the axial mechanical properties of the joint is related to the structural dimensions of the joint.

2) Effect of WRS on axial mechanical properties of joints with the change of structural dimension

① Effect of WRS on axial properties of joints with variation of D

In order to investigate the influence of WRS on the axial mechanical properties of the joint when the diameter D of the hollow sphere changes, the specimens of group 1 and group 2 are selected for analysis. The t and d of the specimens of group 1 and group 2 are exactly the same, and D is 300 and 350 mm respectively. The variation trend of β_K and β_N of the two groups of specimens with D is plotted, as shown in Fig. 15(a).

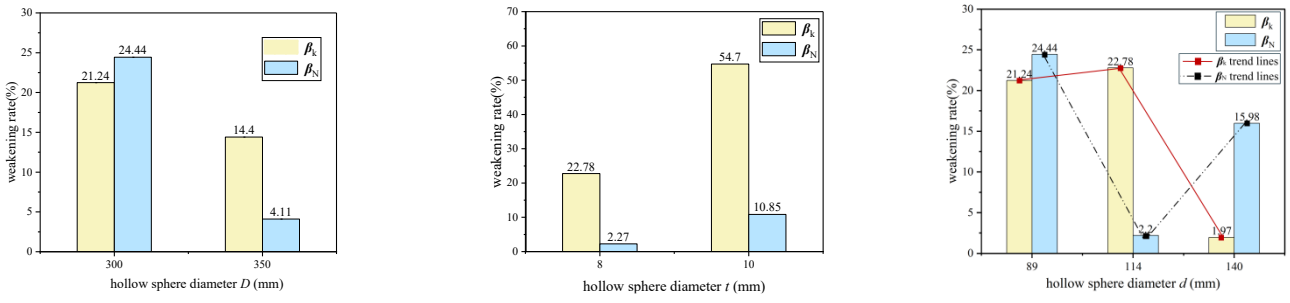

(a) D (b) t (c) d

Fig. 15 Trend of the effect of WRS on the axial mechanical properties of the joints with the variation of geometrical configuration dimensions

As shown in Fig. 15(a), when the hollow sphere diameter D is different, the weakening rate of the WRS on the axial stiffness of joint exceeds 10%, with the maximum weakening of 21.24%; but as D increases, the weakening degree of the WRS on the axial stiffness of joint is decreasing, and the weakening rate when D=300mm is about 1.5 times that when D=350mm. In terms of ultimate bearing capacity, when D=300mm, the weakening of the ultimate bearing capacity by WRS is most obvious, and the weakening rate reaches 24.44%, but as D increases, the weakening degree is also decreasing, and the weakening rate when D=300mm is about 6 times that when D=350mm. It can be seen that the ultimate bearing capacity of small-diameter WHSJ is more affected by WRS, while the influence of WRS on the axial stiffness of joint is insensitive to the change of D.

② Effect of WRS on axial properties of joints with t

Two sets of test results, 3 and 4, are selected to analyze the influence of WRS on the axial mechanical properties of joints as the wall thickness t of hollow sphere changes. The D and d of the two sets of specimens 3 and 4 are exactly the same, and t is 8 and 10 mm respectively. Draw the changing trends of β_K and β_N in groups 3 and 4 with t, as shown in Fig. 15(b). It can be seen from Fig. 15(b) that when the wall thickness t of hollow sphere changes, the WRS weakens the axial stiffness and ultimate bearing capacity of the joint more

significantly, especially the maximum impact on the axial stiffness is as high as 54.7 %; Specifically, the weakening rate at t = 10 mm is approximately 2.4 times that at t = 8 mm. In terms of ultimate bearing capacity, the weakening rate at t = 10 mm is about 5 times that at t = 8 mm. It can be seen that as the wall thickness t increases, the influence of WRS on the axial mechanical properties of WHSJ increases significantly, and as t increases, the influence of WRS on the ultimate bearing capacity of the joint accounts for dominant position, its influence is about twice the influence on the axial stiffness of the joint.

③ Effect of WRS on axial properties of joints with d

In order to examine the influence of WRS on the axial mechanical properties of joints as the steel pipe diameter d changes, the test results of groups 1, 3 and 5 are selected. The D and t of these three groups of specimens are exactly the same, and d is 89, 114 and 140mm respectively. The changing trends of β_K and β_N of each group of specimens with d are shown in Fig. 15(c). It can be seen that when d changes, the maximum weakening rate of the WRS on the axial stiffness of the joint is 22.8%, and the maximum weakening rate on the ultimate bearing capacity of the joint is 24.44%; as d changes, the maximum weakening rate of the WRS on the ultimate bearing capacity of the joint is 22.8%. The degree of influence on axial mechanical properties shows obvious differences. Specifically, when the steel pipe diameter d increases from 89mm to 114mm, the influence of WRS on the axial stiffness of the joint is basically the same, but the weakening rate on the ultimate bearing capacity drops significantly, that is, the weakening rate when d = 89mm is about d = 11 times of 114mm; When the steel pipe diameter d increases from 114mm to 140mm, the degree of weakening of the axial stiffness of the joint by the WRS is significantly reduced, but the degree of weakening of the ultimate bearing capacity is significantly increased, that is, when d = 114mm, the effect of the WRS on the axial stiffness The weakening rate of WRS on the ultimate bearing capacity is about 12 times that of d = 140mm. When d = 140mm, the weakening rate of WRS on the ultimate bearing capacity is about 7 times that of d = 114mm. Overall, as the steel pipe diameter d increases, the degree of weakening of the joint axial stiffness by WRS first increases and then decreases, and the degree of weakening of the ultimate bearing capacity first decreases and then increases.

4.2.3. Destruction mode

As shown in Fig. 16, the destruction modes of each group of specimens are not exactly the same. They can be roughly divided into three categories: The first category is that when the hinge support cannot rotate around the support x-axis and the axial force is mainly eccentric along the y-axis, the sphere-pipe connection area of the hollow sphere will generate a large shear force during loading. SJ1 and SJ2 in Fig. 16 are such cases; The second category is when the axial force is mainly eccentric along the x-axis direction, because the hinge support can rotate in this direction (around the y-axis), the steel pipe tilts during loading, and one side of the weld is concave and the other side is convex during destruction. SJ1-D, SJ4 and SJ5 belong to this category; The third category is that the eccentricity is always small during loading, the specimen is loaded to destruction, the steel pipe is evenly sunken into the hollow sphere, and punching shear failure mainly occurs. SJ2-D, SJ3, SJ3-D, SJ4-D and SJ5-D all belong to this category. In order to accurately examine the eccentricity of each group of specimens during the test, 4 groups of strain gauges are symmetrically arranged on the upper and lower steel pipes. Taking SJ1 as an example, according to the strain collected from the steel pipe during loading, the initial eccentricity of the joint is calculated to be only 1.5 mm. The other groups of specimens also had different degrees of initial eccentricity, but their influence is not significant compared with the structure dimension of joint.

Fig. 16 Actual view of specimen destruction

Note: x-x in the Fig.16 indicates observation along a direction perpendicular to the y-y axis shown in Fig. 12; y-y indicates observation along a direction perpendicular to the x-x axis shown in Fig. 12.

In addition, it can be seen from Fig. 16 that for the test specimens in the test group, namely, SJ1~SJ5 specimens, all three destruction modes may occur; But for the control group specimens, except SJ1-D, all belong to the third category of destruction mode. The second category of destruction occurred in specimen SJ1-D, mainly because the loading process produced a large eccentricity along the x-axis. It can be seen that when each specimen has a certain initial eccentricity, the test group specimens and the control group specimens show significantly different destruction modes, indicating that the initial eccentricity is not the only factor of the destruction mode of specimen. The WRS at the sphere-pipe connection weld also has a certain influence on the destruction mode of the joint. The specific influencing mechanism is as follows:

When the WRS is not considered or the residual stress value is small, the destruction of the hollow spherical joint under axial load begins at the outer surface of the sphere-pipe connection. After the outer surface reaches yield, a plastic zone is formed and develops to the inner surface. As the load increases, the inner surface also enters the plastic stage and expands to the outer surface. When the plastic zones of the inner and outer surfaces converge, the hollow spherical joint undergoes uniform shear failure [23], as shown in Fig. 17(a). When there is non-negligible WRS on the hollow spherical joint, the existence of WRS will interfere with the shear stress distribution on the punched surface, resulting in unequal distribution of shear stress on the circumferential shear surface of joint. The unevenly distributed WRS and the stress generated by the external load will cause the outer surface of the weld starting point to yield first, and then gradually expand to the inner surface, while other circumferential areas still have a certain resistance and no large plastic deformation occurs. Under the combined effect of this circumferential uneven deformation, the hollow spherical joint will eventually be damaged by bias pressure, and the distribution of WRS on the punched surface is larger, as shown in Fig. 17(b). The research team found in the previous studies that the distribution of WRS on the punched surface of the other groups of specimens is generally similar to that of SJ1, and there is only a difference in value with the structure dimension of joint. Therefore, the specimens of the test group in Fig. 16 all suffered different degrees of bias pressure damage under the influence of WRS.

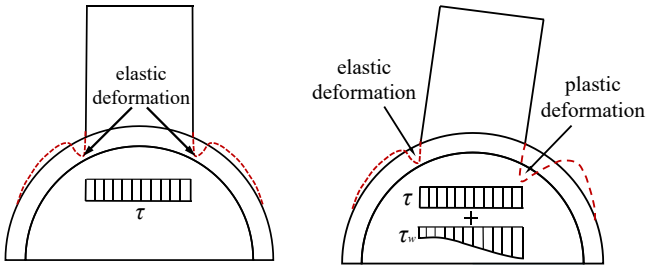

(a)Uniform deformation (b) Uneven deformation

Fig. 17 Schematic diagram of the effect of WRS on the damage mode of the specimen

5. Conclusion

The large number of sphere-pipe connection welds on WHSJ will cause complex WRS in the joints. This paper conducts theoretical derivation and experimental research on the influence of WRS on the axial mechanical properties of WHSJ. The main research conclusions are as follows:

1) The influence mechanism of WRS on the axial stiffness and axial compressive bearing capacity of WHSJs is clarified through theoretical derivation. Theoretically, WRS can reduce the axial stiffness of WHSJ by about 8.9%~36.8%, and the axial compressive ultimate bearing capacity by about 10.5%~87.2%.

2) The axial bearing performance test of WHSJ is carried out. The results show that WRS can reduce the axial stiffness of WHSJ by about 1.97%~54.7%, and the axial compressive ultimate bearing capacity by about 2.27%~24.4%, and will affect the destruction mode of the joint.

3) The influence of WRS on the axial mechanical properties of the joint as the change of structural dimensions of joint is revealed. The influence of WRS on the axial stiffness and axial compressive ultimate bearing capacity of the joint decreases with the increase of the diameter D of hollow sphere, and increases with the increase of the wall thickness t. As the diameter d of the steel pipe increases, the influence on the axial stiffness first increases and then decreases, while the influence on the axial compressive ultimate bearing capacity first decreases and then increases.The influence of steel pipe diameter d on the axial mechanical performance of WHSJ follows a non-monotonic trend. With increasing d, its effect on axial stiffness initially intensifies then diminishes, while its impact on axial compressive ultimate bearing capacity first decreases and subsequently increases.

Acknowledgments

Supported by the Science and Technology Research Program of Chongqing Municipal Education Commission (Grant No. KJQN202403002)

Reference

[1] Liu X.L. and Chen Z.H., Connection between spherical tubes of welded hollow spherical joints of space truss, J.Steel Const, 04, (1991) 52-54. (in Chinese).
[2] Wang X., Dong S.L. and Wan H.Y., Analysis of influence of welding spherical joint stiffness on internal force and deflection of grid, J.Spatial Structures, 2(4),(1996) 34-40 (in Chinese).
[3] Zhang J.L. and Zhao J.C., Influence of joint stiffness on buckling of short-line linear single-layer spherical shell, J.Building Technique Development, 30(3), (2003) 8-9 (in Chinese).
[4] Zhang J.L. and Zhao J.C., The influence of joint stiffness exerted on the stability of Kiewite-type singlelayer reticulated shells, J. Spatial Structure, 10(2), (2004) 43-45, (in Chinese).
[5] Kang J. and Song Z.S., The influence of joint stiffness on the stability of geodesic single-layered reticulated shells with initial in perfection, J. Sichuan Building Science, 34(1), (2008) 42-46, (in Chinese).
[6] Kang J., Zhao J. and Song Z.S., The influence of joint stiffness on the stability of hyperbolic paraboloid reticulated shells with initial in perfection, J.Low Temperature Architecture Technology, (6), (2005) 47-49, (in Chinese).
[7] Li F., Lou Q.L. and Liu T., Study on static performance of cylindrical giant grid structure based on node stiffness, J. Journal of Xi'an University of Architecture and Technology:Natural Science Edition, 46(5), (2014) 682-686, (in Chinese).
[8] Su Y.H., Research on the Effect of Joints Stiffness on the Stability of Reticulated Shells, D. College of Civil Engineering, Southeast University, Nanjing, China, (2005).(in Chinese).
[9] Yan X.Y., Duan Y. and Zhang Y.X., Chen Z.H., Study on compressive bearing capacity and axial stiffness of welded hollow spherical joints with H-shaped steel member, J. Engineering Structures, 203, (2020) 109821.
[10] Yan X.Y., Duan Y. and Cheng Z.H., Liu H.B., Flexural capacity and bending stiffness of welded hollow spherical joints with H-beams, J. Engineering Structures, 24(05), (2021) 1024-1039.
[11] Liu H.B., Ying J.J. and Chen Z.H., Zhou Y., Ultimate tensile and compressive performances of welded hollow spherical joints with H-beam, J.Journal of Constructional Steel Research, 150, (2018) 195-208.
[12] Zhao Z.W., Dai B.Z. and Xu H., Li T.H., Bending capacity of corroded welded hollow spherical joints with considering interaction of tension force and bending moment, J.Structures, 34, (2021) 2656-2664, 10.
[13] Han Q.H., Liu Y.M. and Xu Y., Stiffness characteristics of joints and influence on the stability of single-layer latticed domes, J.Thin-Walled Structures, 107 (2016) 514-525.
[14] Yan X.Y., Zhang Q.W. and Qi G.C., Study on bending stiffness of welded hollow spherical joints based on bending loading states, J. Chinese Journal of Applied Mechanics, 38(01), (2019) 35-44, (in Chinese).
[15] Zhao Z.W., Liu H.Q. and Liang B., Bending capacity of corroded welded hollow spherical joints, J. Thin-Walled Structures, 127, (2018) 523-539.
[16] Lu J., Liu H.B. and Cheng Z.H., Behavior of welded hollow spherical joints after exposure to ISO-834 standard fire, J. Journal of Constructional Steel Research, 140, (2018) 108-124.
[17] Huang B.S., Lu M. and Cao Y.F., Yang F., Experimental study on residual performance of welded hollow spherical joints subjected to axial compression after a fire, J.Structures, 30, (2021) 996-1005.
[18] Liu H.B., Lu J. and Cheng Z.H., Residual behavior of welded hollow spherical joints after exposure to elevated temperatures, J. Journal of Constructional Steel Research, 137, (2017) 102-118.
[19] Liu H.B., Zhao Y. and Wang L. Cheng Z.H., Axial compression properties of welded hollow spherical joints with H-beams under high temperature, J. Journal of Constructional Steel Research, 169 (2020) 10605.
[20] Liu H.B., Zhang Y.J. and Wang L., Cheng Z.H., Mechanical performance of welded hollow spherical joints at elevated temperatures, J.ADVANCED STEEL CONSTRUCTIO 16(1), (2020) 1-12.
[21] Luo Y.F. and Sheng Z.Y., Effects of the joint size of the reticulated shell on its loading capacity, J. Journal of Tongji University, 1(23), (1995) 21-25, (in Chinese).
[22] Dong S.L., Xing L. and Zhao Y., Load-carrying capacity and practical calculation method of welded hollow spherical joints connected with square steel tubes, J. Journal of Building Structures, 26(6), (2005) 27-37, (in Chinese).10.3321/j.issn:1000-6869.2005.06.005.
[23] Dong S.L., Tang H.J. and Zhao Y., Loadcarrying capacity and practical calculation method for welded hollow spherical joints subject to combine axial force and bending moment, J. Journal of Civil Engineering Society, 38(1), (2005) 21-30, (in Chinese).
[24] Liao J. and Zhang Y.G., The study of bilinear model for loading-deformation curve of welded hollow spherical joints, J. Spatial Structures. 16(02), (2010) 31-38. (in Chinese).
[25] Wang X., Dong S. and Wan H.Y., Finite element analysis of the stiffness of welded ball joints, J.Journal of Zhejiang University (Engineering Edition). (01), (2000) 79-84.
[26] Zhao Z.W., Zhu H. and Chen Z.H., Mechanical behavior of single-layer reticulated shell connected by welded hollow spherical joints with considering welding residual stress, J. Welding in the World, 60(1), (2016) 61-69.
[27] Yan R.Z., Zhang C.L. and Wang S., Distribution of residual stress in the sphere-pipe connection welds of welded hollow spherical joints, J. Advanced Steel Construction. 19(3), (2023) 262-272.
[28] Yan R.Z., Yu Z.Y. and Wang S., Liu J.Q., Influence of welding residual stress on bending resistance of hollow spherical joints, J. Journal of Constructional Steel Research. 208, (2023)
[29] Jin X.Q. Distribution of WRS in Hollow Sphere Joints and its Influence on Joint Axial Stiffness, D. Chongqing Jiaotong University, Chongqing, China, (2019). (in Chinese).
[30] Huang K.Z. Plate and shell theory, M. Tsinghua University Press. Beijing. China, (1987).
[31] Ministry of Housing and Urban-Rural Development of the People's Republic of China. Technical specification for space grid structure: JGJ 72010, S. China Construction Industry Press, Beijing China, (2010).